Transcranial Ultrasound Estimation of Viscoelasticity and Fluidity of the Soft Matter

Jianjun Yu,[1] Hao Guo,[1] Meng Han,[1] Fan Wang,[1] Ayache Bouakaz,[2] Hongmei Zhang,[1,*] and Mingxi Wan[1,†]

[1] *The Key Laboratory of Biomedical Information Engineering of Ministry of Education, Department of Biomedical Engineering, School of Life Science and Technology, Xi'an Jiaotong University, Xi'an, China*

[2] *UMR 1253, iBrain, Université de Tours, Inserm, Tours 37000, France*

(Received 23 June 2021; revised 12 November 2021; accepted 24 December 2021; published 1 February 2022)

In the fields of geology, materials and biomedical engineering, the noninvasive and accurate estimation of the dynamic mechanical properties of the soft matter enclosed in a rigid shell induced by a low-frequency vibration is worthy of exploration. The addition of fluidity on the basis of viscoelasticity to describe the properties of the soft matter, especially when containing a large amount of water, may be of great value in the detection of crustal movement, material structure, and early cerebral diseases. In the biomedical field, since the influence of the skull on ultrasound is unknown for viewing the propagation of the transcranial shear wave, it is challenging to obtain the mechanical properties of the brain tissue with the skull using the transcranial ultrasound. In this study, the propagations of the transcranial shear wave within the brain tissue induced by an external low-frequency vibration are presented by finite-element-method simulation. This experiment achieved a transcranial ultrasound estimation and differentiation of viscoelasticity and fluidity of brain phantoms enclosed in the skull using the low-frequency vibration and Kelvin-Voigt fractional derivative modeling, and the estimation results are consistent with the nontranscranial ones. These results represent a great potential in the estimation of viscoelasticity and fluidity of the soft matter under different boundary constraints in various areas.

DOI: 10.1103/PhysRevApplied.17.024001

I. INTRODUCTION

The noninvasive estimation of the nonlinear mechanical properties of the soft matter enclosed in a rigid shell is of considerable interest in various fields [1–3]. In the soft matter, especially that with high water content, these properties vary with the molecular arrangement, cross-linking density, and properties of the interstitial fluids, which may be susceptible to modifications during processes like crustal movement, tissue inflammation, and material reordering. These properties can be extracted when an appropriate constitutive model fits the data acquired from the displacement field induced by low-frequency (LF) vibration [3–5]. The current mechanic community prefers classical constitutive models, such as the Maxwell model, the Kelvin-Voigt model, and the standard linear solid model. However, these elementary models for viscoelasticity description fail to accurately capture the shear dynamic behavior of the soft matter [6,7], and this dilemma can be solved by increasing the complexity of the constitutive model. Instead of increasing the number of model parameters, a better alternative is to employ the Kelvin-Voigt fractional derivative (KVFD) model [7,8]. KVFD is an elegant model offering a more compact set of viscoelastic and fluidic properties for characterizing the soft matter [9]. In the biomedical field, the feasibility of the extended KVFD to assess viscoelasticity and fluidity of the brain tissue enclosed in the human skull is worth exploring, and these properties can provide key information for the diagnosis of cerebral diseases at an early stage and monitor the progression of the disease treatment [10,11].

Two noninvasive ways are available in the biomedical field to excite the shear wave within the tissue: external LF vibration [12] and acoustic radiation force (ARF) [13]. The frequency of the shear wave generated by ARF has a broad bandwidth, making it difficult to control the propagation of the shear wave at a single frequency. On the other hand, the frequency of the shear wave induced by an external LF vibration is narrowband, thus facilitating the propagation of the shear wave at single frequency. In this way, the viscoelastic and fluidic properties can be related

*Corresponding author. claramei@mail.xjtu.edu.cn
†Corresponding author. mxwan@xjtu.edu.cn

to the shear wave speeds at different frequencies by KVFD modeling.

The shear wave within the brain tissue can be detected by biomedical imaging methods, such as magnetic resonance elastography (MRE) [14] or ultrasound shear-wave imaging (SWI) [15–17]. MRE is able to measure the mechanical properties of the soft matter [18], then also extended to the brain tissue [19,20] in a noninvasive manner. MRE in clinical practice is used to estimate the elasticity of the brain tissue by placing a vibrating plate under the patient's head or in the patient's mouth and connecting it to a mechanical actuator [14,19,20]. However, the use of MRE is limited and restricted only to dedicated clinical centers. Moreover, the long acquisition time of MRE limits its usage as a routine test for brain research [14], while SWI has a better temporal resolution allowing the dynamic estimation of the brain elasticity within a single cardiac cycle [15]. Currently, SWI has already been used in clinical practice to evaluate the tissue elasticity in a variety of soft tissues such as liver [21], thyroid [22], breast [23], and prostate [24]. However, SWI is rarely applied on noninvasive transcranial human brain tissue, which can be due to three reasons. Firstly, the attenuation coefficient of ultrasound in the skull is very strong due to the mismatched acoustic impedance [25]. Secondly, the propagation of the transcranial shear wave is complex due to the rigid boundary constraint of the skull. Thirdly, the three-dimensional (3D) wave propagation in the brain can be acquired by MRE, while the transcranial ultrasound imaging can only display a two-dimensional (2D) section of the brain tissue. Therefore, the position of the LF vibration used in MRE is not suitable for transcranial ultrasound, and an appropriate position should be reselected for transcranial ultrasound to estimate the viscoelasticity and fluidity of the soft matter.

Inspired by MRE, the external LF vibration is used in this study to excite the shear wave and estimate the mechanical properties of the soft matter enclosed in the skull. The propagation of the shear wave within the brain tissue is simulated under different boundary constraints referred to as the absence or presence of the skull, to better understand the influence of the skull on the propagation of the transcranial shear wave and provide the appropriate position of the LF vibration and ultrasound probe in the following experiments. A method for the noninvasive transcranial ultrasound shear-wave imaging is developed. The external LF vibration and the ultrasound probe each placed on each side of the temporal window are designed for transcranial ultrasound. The LF vibration at different frequencies is used in this experiment to induce the shear wave within the brain phantom. The noninvasive estimation of viscoelasticity and fluidity are validated by brain phantoms using transcranial ultrasound shear-wave imaging induced by external variable LF vibration and KVFD modeling.

II. SIMULATION OF SHEAR-WAVE PROPAGATION

The shear-wave propagation within the brain tissue can be simulated by the finite-element analysis, which is conducted via COMSOL Multiphysics (release 5.5, COMSOL Inc., USA). The shear-wave propagations within the brain tissue with free boundary and enclosed in the human skull are simulated under an external LF vibration. In the simulation, 50 cycles of sinusoidal force are applied to an elastic film to act as an external LF vibration. The frequency of vibration is set from 100 to 300 Hz in 50-Hz steps. The shape of the film is obtained by the calculation of the Boolean difference between the film and brain tissue in the boundary-free constraint, while between the film and skull in the enclosed human skull constraint. This approach allowed the close attachment of the film to the brain tissue or skull. The elastic film is placed near the temporal window. The temporal window of the skull is the maximum radius of the curvature and the thinnest part of the skull [26]. The details of the simulation setup are shown in Figs. 1(a) and 1(d). The mechanical parameters of the skull, brain, and film are listed in Table I [17,27]. The dura mater, spinal fluid, and other substances are ignored. The time step of the simulation is 1 ms.

Taking the LF vibration of 100 Hz as an example, the shear-wave propagation within the brain induced by the nontranscranial and transcranial LF vibration is shown in Figs. 1(b)–1(c) and 1(e)–1(f). As regards the nontranscranial LF vibration, the brain tissue is free from any boundary, and the LF vibration directly acts on the tissue. Figures 1(b) and 1(c) show that the shear wave propagated in an arc along the X axis, which is similar to the propagation within phantom [18,28,29] and tissue [12,29] in the shear-wave elastography. As regards the transcranial LF vibration, which is different from the former one, the brain tissue is enclosed in the skull on which the LF vibration acts. In this case, the propagation becomes complicated, as shown in Figs. 1(e) and 1(f). At 6 ms after the beginning of the vibration, the arc wave propagated along the X axis in the brain at the temporal window. At 12 ms after the beginning of the vibration, the LF vibration spread along the skull from the temporal window to the parietal bone. At this time, the propagation of the transcranial shear wave was different from the nontranscranial shear wave. The transcranial shear wave propagation was composed of two waves forming interference in the brain tissue: the one generated from the temporal window was spreading in an arc along the X-axis, and the other one generated from the parietal bone is spreading along the Z axis. The propagation directions of these two waves are nearly perpendicular. Since the propagation direction of the shear wave is along the X and Z axis, the X-Z section is selected as a better observation section to detect the propagation of the shear wave. The LF vibration and transcranial ultrasound

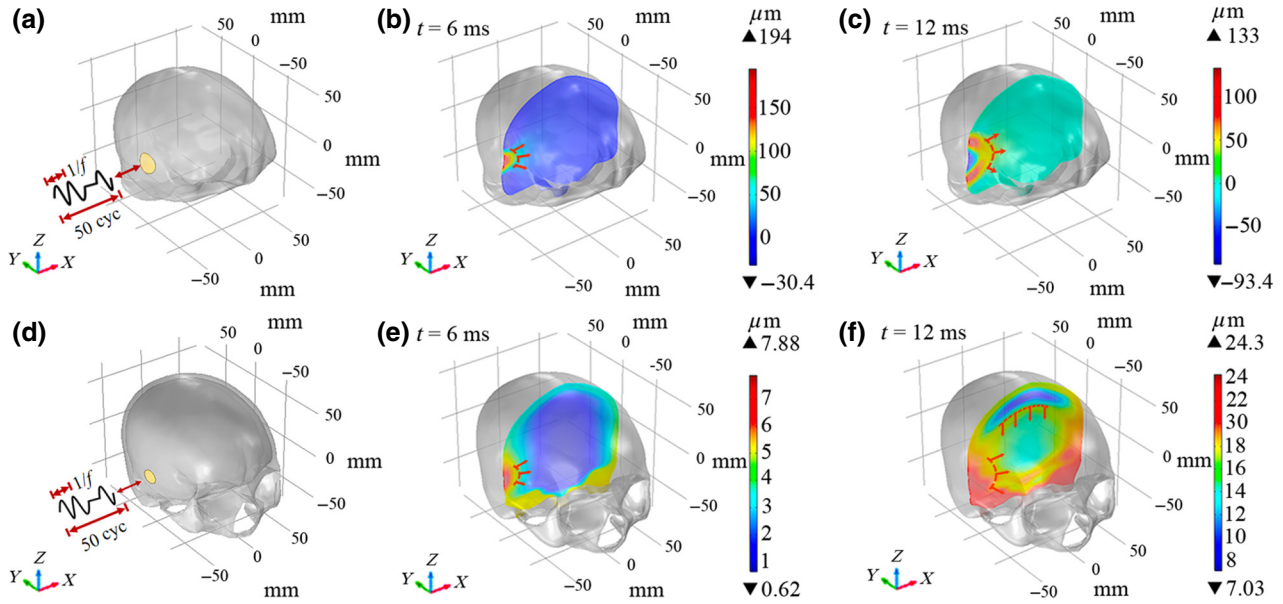

FIG. 1. Simulation of the shear-wave propagation within the brain tissue induced by the LF vibration. The color bar represents the amplitude of the displacement. The simulation models are, respectively, the brain tissue with free boundary (top row) and with the skull (bottom row). (a),(d) Details of the simulation setup. The yellow curved surface represents the film. The film is subjected to a sinusoidal force, and the frequency of the force is from 100–300 Hz in the 50-Hz steps. f (Hz) represents the frequency of the force. (b),(c) Shear wave propagating in an arc along the positive X axis at 6 and 12 ms after film vibration, respectively. (e) At 6 ms after the film vibration, the propagation of the transcranial shear wave is similar to that in (b). (f) The propagation of the shear waves from two directions (X and Z axis) is clearly observed at 12 ms after film vibration.

are each placed on each side of the temporal window in the following experiment, which is an appropriate position to view the transcranial shear wave and estimate the shear-wave speed by transcranial ultrasound.

III. EXPERIMENTAL METHODS

A. Phantom with skull models

The 3D-printed skull models with matched acoustic properties are designed using an optimal material after comparing the acoustic properties of a real skull with different commercially available printing materials [30]. The ultrasound attenuation coefficient and ultrasound speed of the skull model printed by polylactic acid (PLA) material is similar to that of the real human skull with porosity. Thus, the PLA material is used to print the cubic skull model and whole skull model in this study. The cubic model is composed of a five-sided $10 \times 10 \times 10$ cm^3 cube, and the thickness is 2.0 mm, which is the average thickness at the acoustic bone window [26]. The cubic skull model is used to preliminarily verify the feasibility of the experiment. The geometric shape of the enclosed whole skull model is obtained by 3D printing of the CT-reconstructed skull, and the shape and thicknesses are close to the human skull to further validate the efficiency of the method.

TABLE I. Parameters of the materials in the simulation.

	Skull	Brain	Film
Young's module (MPa)	6900	0.013	280
Density (kg/m^3)	1080	1000	2200
Poisson's ratio	0.3	0.485	0.4

Both skull models are filled with gelatin-agar phantom to imitate the brain tissue ignoring the intracranial pressure. The brain phantoms are composed of gelatin and agar powders mixed with hot water (65 °C). The agar powder (1%) is used as a scatterer for phantoms. Three different gelatin concentrations (4%, 6%, and 8%) are used for brain phantoms in the experiment with different viscoelastic and fluidic properties.

B. The transcranial ultrasound SWI system

The transcranial ultrasound SWI experiment setup is shown in Fig. 2. The excitation sine signal is generated from a waveform generator (AWG420, Tektronix), and amplified by an audio power amplifier (FPA1016, FeelTech, China). Then, the LF loudspeaker (DL65TZB-01, Guanyin, China) is excited to vibrate. The frequencies of the LF loudspeaker vibration are between 100 Hz and 300 Hz, with steps of 50 Hz. The LF loudspeaker is triggered by an ultrasound imaging system to synchronize the data acquisition with the LF loudspeaker vibration. The loudspeaker is affixed to a tube by a plexiglass dome used to connect hermetically both parts. The tube is made of

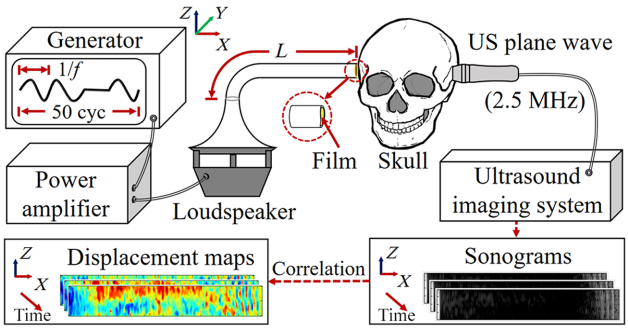

FIG. 2. Experimental system of the transcranial ultrasonic shear-wave imaging. The excitation is a continuous LF sine wave. f (Hz) represents the frequency of the continuous LF sine wave. The tube and the probe are kept at the same height in the Z axis. L (m) represents the length of the tube. The details of the tube's nozzle are shown in the red circle, and the yellow curved surface represents the film. The displacement maps are retrieved through the correlation of the subsequent transcranial ultrafast plane-wave images.

polyvinyl chloride and its inner diameter is 18 mm. The length L (m) of the tube varied with the frequency f (Hz) of vibration, according to the standing-wave equation $L = (2n-1)^* c/4f$ $(n = 1, 2\ldots)$. c (m s^{-1}) is a constant, representing the speed of the sound in the air. The shape of the tube nozzle is determined by Boolean difference calculation of three-dimensional graphics, so that the tube nozzle is closely fitted to the temporal window of the skull. A 30-μm-thick elastic film is connected at the nozzle of the tube, and the material of the film is biaxially oriented polypropylene. The vibration of the loudspeaker spread along the tube and drove the film at the nozzle to vibrate. The film vibration is exerted on the skull and induced the propagation of the transcranial shear wave in the brain phantom.

The suitable frequency for the transcranial ultrasound is approximately below 3 MHz due to a great attenuation of the high-frequency ultrasound within the skull [30]. Considering the imaging resolution and the ultrasonic attenuation, a P4-2 probe with 2.5 MHz is selected to detect the motion of the brain phantom through the skull using a Verasonics ultrasound imaging system (Vantage 256, Verasonics Inc., Kirkland, WA, USA). The probe is placed at the temporal window. The temporal window is the thinnest, thus, the attenuation of the ultrasound is minimal. The temporal window is relatively flat, and the probe could be placed vertically to the skull, to minimize the ultrasound attenuation. When the shear wave propagated in the brain tissue for a period of time, the propagation became more complex, with a phase distortion due to the strong reflection interface of the skull. rf echoes should be acquired within 100 ms after the loudspeaker vibration in the experiment. Therefore, the ultrafast frame rate is achieved by reducing the emission mode to a single, plane wave in sonification. The frame rate for the acquisition of echographic images is set at 1000 Hz. The sampling rate of rf echoes is increased from 4 times (10 MHz) to 10 times (25 MHz) of transcranial ultrasonic frequency to ensure the accuracy of the displacement detection in the brain phantom. All the backscattered signals are stored in a memory, and then transferred to a computer for offline processing.

C. Estimation of viscoelasticity and fluidity

The rf signals are acquired while the transcranial shear waves are propagating, and the first frame is used as the reference echographic image of the medium. The X displacement is estimated using a cross-correlation algorithm by comparing the correlation between two frames of images. The cross-correlation algorithm is robust to extract the displacement information from the low signal-to-noise ratio rf signals. Thus, even though the rf signals of the transcranial ultrasound have an attenuation due to the skull, the X displacement can still be estimated by the cross-correlation algorithm. The rf lines are segmented by depth X into approximately 2-mm slices with a 50% overlap. The rf lines and displacements are both filtered using a spatial-time filter to increase the signal-to-noise ratio [31,32]. The precision is improved by applying the parabola interpolation method to the displacement estimation.

The nonlinear mechanical properties of the tissue can be depicted from the tissue displacements. The equation of the displacement for small perturbations regarding an operating point can be used for an isotropic, homogenous, viscoelastic compressible medium [33]:

$$(\lambda + \mu)\nabla\nabla\cdot\mathbf{u} + \mu\nabla^2\mathbf{u} = \rho\frac{\partial^2\mathbf{u}}{\partial t^2}, \tag{1}$$

where ρ is the density of the medium, $\mathbf{u}$ is the displacement vector, and μ and λ are the Lamé constants of the medium.

After applying the KVFD model, the fractional order viscoelasticity is the following [7]:

$$\mu = \mu_0 + \mu_\alpha\frac{\partial^\alpha}{\partial t^\alpha}, \quad 0 < \alpha \le 1. \tag{2}$$

The nonlinear mechanical properties of the tissue can be depicted by viscoelastic models, which relate the shear-wave speeds and the complex modulus. The shear-wave speeds at variable frequencies are related to the real storage and imaginary loss parts of the shear modulus μ_R and μ_I, respectively:

$$c_s = \sqrt{\frac{2}{\rho}\frac{\mu_R^2 + \mu_I^2}{\mu_R + \sqrt{\mu_R^2 + \mu_I^2}}}. \tag{3}$$

In the case of the KVFD model,

$$\mu_R = \mu_0 + \mu_\alpha \omega^\alpha \cos\left(\frac{\pi}{2}\alpha\right), \quad \mu_I = \mu_\alpha \omega^\alpha \sin\left(\frac{\pi}{2}\alpha\right), \tag{4}$$

where μ_0 (Pa) is the elastic modulus, μ_α (Pa s^α) is the viscous coefficient, and α is the unitless real number between 0 and 1 that defines the derivative order representing the fluidic property.

The shear-wave speed is estimated using the linear regression of the evolution of the phase delay of the strain estimation as a function of depth at the center frequency of the LF vibration. It is reported that there is no difference between the phase speed and the shear-wave speed as long as the diffraction effects and dissipation can be ignored [34]. Then the viscoelasticity and fluidity could be estimated using the KVFD model and shear-wave speeds at variable frequencies.

D. Statistical analysis

Statistical analysis is performed to confirm the feasibility of the transcranial SWI induced by the proposed method. The difference in viscoelasticity and fluidity with different concentrations of gelatin brain phantom (4%, 6%, and 8%) enclosed in the cubic skull model are compared. Then, taking the 6% gelatin brain phantom as an example, the consistency of the viscoelasticity and fluidity of the phantom under three boundary constraints is evaluated by the intragroup correlation coefficient (ICC) [35]. The three different boundary constraints are referred to as the phantom in the free boundary, enclosed in the cubic skull model and enclosed in the whole skull model, respectively.

IV. RESULTS AND DISCUSSION

Figure 3(a) shows the shear-wave propagation within the 6% gelatin brain phantom enclosed in the cubic skull model at 18, 46, and 48 ms after the loudspeaker vibration at 100 Hz. The top row shows the transcranial shear wave propagated in the brain-tissue phantom in a quasi-circular arc along the X axis at the temporal window. The second and third row show another shear wave propagated along the Z axis from the top skull. The interference of the two shear waves propagated in nearly perpendicular direction is shown. The propagation in the experiment agreed with the simulation. The phase of the shear wave along the Z axis at the depth of 10 mm shows a nonlinear way and the phase delay is very small, indicating the occurrence of the wave interference phenomenon [Fig. 3(b)]. As the shear wave propagated, the energy of the shear wave in an arc along the X axis decreased due to the nonlinearity of the phantom. The shear-wave energy propagating along the Z axis above the depth of 20 mm is much greater than that along the X axis, thereby the wave interference is weakened, and the speed can be estimated by the slope of the phase shift. The transcranial shear-wave speed (1.61 m s^{-1}) along the Z axis is shown in Fig. 3(c) at the depth of 50 mm.

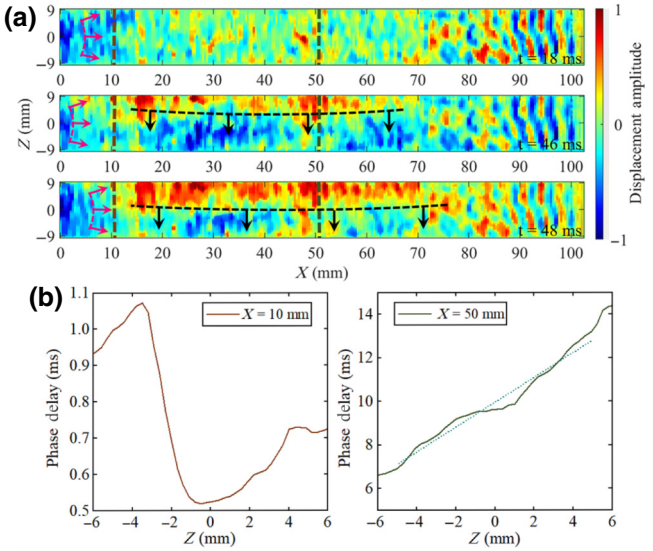

FIG. 3. (a) X-axis displacement induced by the LF transcranial vibration at 100 Hz. The multilayer blue and red stripes at the depth of 80–100 mm are caused by multiple reflections of the ultrasound passing through the cubic skull model. The color bar represents the amplitude of the displacement. The red and black arrows show the directions of the shear-wave propagation. Propagating transcranial shear wave at three time steps (18, 46, and 48 ms). (b) Phase delay of shear wave along the Z axis at the depth of 10 mm. (c) Phase delay of shear wave along the Z axis at the depth of 50 mm. The green dotted line represents the linear curve of the shift phase.

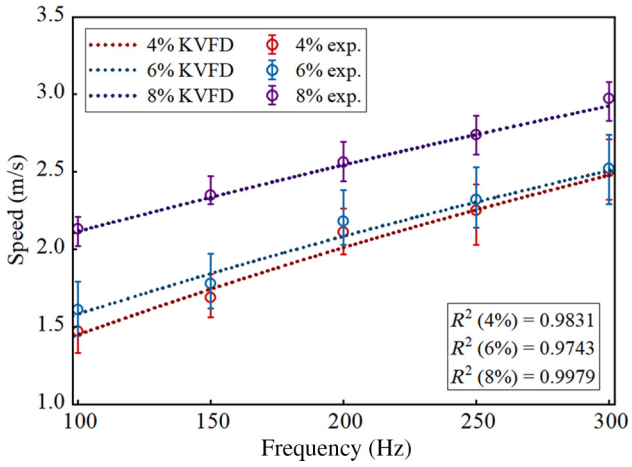

FIG. 4. Shear-wave speeds within gelatin phantoms (4%, 6%, and 8%) along the Z axis at different frequencies are fitted by the KVFD model. The dots represent the experimental shear-wave speeds that actually represent the average speeds, with the maximum deviation indicated by the error bars. The dotted lines represent the curve fitting by the KVFD model, with 95% confidence interval.

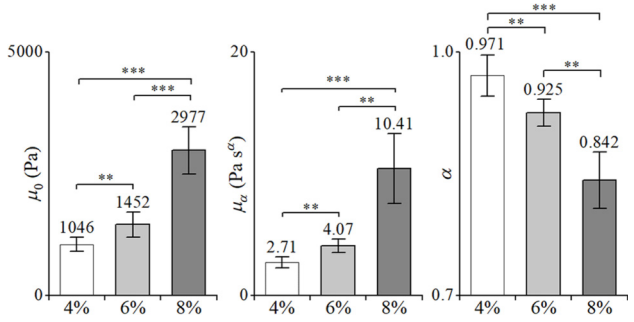

FIG. 5. Comparisons of the elasticity μ_0 (Pa), the viscosity μ_α (Pa s$^\alpha$), and the fluidity α for the 4%, 6%, and 8% gelatin brain-phantom groups. Results are expressed as mean ± standard error of the mean. $**p < 0.01$; $***p < 0.001$.

According to Eqs. (3) and (4), the shear-wave speeds within gelatin phantoms along the Z axis at different concentration (4%, 6%, and 8%) and different frequencies are fitted by the KVFD model, and the initial values of the parameters are set within the limits to avoid local minima. Figure 4 shows the fitting results of gelatin phantoms (4%, 6%, and 8%), and the R^2 between the optimal solution and the deviation is 0.9831, 0.9743, and 0.9979, respectively. The viscoelastic and fluidic properties of gelatin phantoms are estimated and shown in Fig. 5. The differences among the three groups are significant ($p < 0.001$) based on the elastic modulus μ_0 (Pa), viscous coefficient μ_α (Pa s$^\alpha$) and fluidic property α. The μ_0 (Pa) and μ_α (Pa s$^\alpha$) increases with the increase of the gelatin concentration, whereas α shows an opposite tendency. No significant difference in shear wave speeds is observed between the groups of 4% and 6% gelatin phantom, but both viscoelasticity and fluidity are significantly different ($p < 0.01$). Thus, the parameters show a good quantitative prediction, which confirms the validity of the proposed approach.

Furthermore, the viscoelasticity and fluidity of the brain phantom enclosed in the whole skull model are measured to verify the effectiveness of the method. The displacement of the brain phantom induced by the transcranial LF

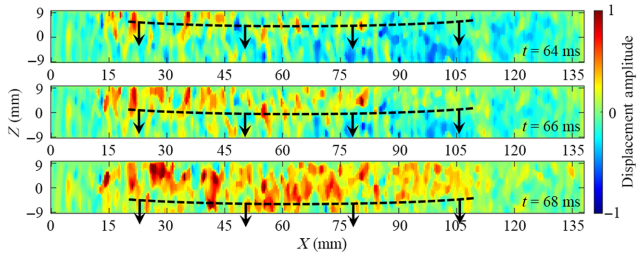

FIG. 6. X-axis displacement induced by the LF transcranial vibration at 100 Hz in the three time periods (64, 66, and 68 ms). The shear waves within the 6% gelatin brain phantom in the whole skull model are shown. The waves propagated along the Z axis, which is the direction indicated by the black arrow.

TABLE II. Viscoelastic and fluidic parameters of the 6% gelatin brain phantom with three boundary constraints.

Boundary constraints	μ_0 (Pa)	μ_α (Pa s$^\alpha$)	α
Free boundary	1305.0	4.357	0.917
Cubic skull model	1452.2	4.07	0.925
Whole skull model	1271.0	4.096	0.926

vibration is detected by transcranial ultrasound, and the viscoelastic and fluidic properties of the phantom can be estimated. The shear waves at 100 Hz propagated along the Z axis within the 6% gelatin brain phantom at a velocity of 1.5 ± 0.15 m s^{-1} are shown in Fig. 6.

The viscoelasticity and fluidity of the 6% gelatin brain phantom are compared under three different boundary constraints (free boundary, cubic skull model, and whole skull model) to verify the reliability of the properties estimated by the method, which is shown in Table II. A statistical analysis of the consistency of the ICC is carried out for these properties among the three groups. The value of the ICC is 0.995 (95% confidence interval: 0.947–1.000), suggesting that the results are highly consistent and indicating the high credibility of the viscoelastic fluidity obtained by this method. That is to say, the skulls failed to affect the shear-wave speed within the brain tissue enclosed in the skull, when the effect of the intracranial pressure is ignored.

V. CONCLUSION

In conclusion, this work achieves a noninvasive transcranial ultrasound estimation of the viscoelasticity and fluidity of the brain phantom. Firstly, the transcranial and nontranscranial shear-wave propagation within the brain tissue is simulated. The simulation results show the difference between transcranial and nontranscranial shear-wave propagation. An interference of the two waves in the brain with nearly perpendicular directions exist in transcranial shear-wave propagation, one in an arc along the X axis and the other along the Z axis, while the nontranscranial shear wave propagated in an arc along X axis in the brain tissue. Next, the optimal observation section of the transcranial ultrasound is selected according to the simulation results. In this experiment, the viscoelastic and fluidic properties of the brain phantoms with different concentrations of gelatin (4%, 6%, and 8%) enclosed in the skull can be accurately estimated, and even slightly different properties can be distinguished. Viscoelastic and fluidic properties of the brain phantom enclosed in the skull model and with the free boundary estimated by the proposed method are also compared, and the results are highly consistent (ICC = 0.995). In other words, the estimation of viscoelasticity and fluidity is consistently estimated by this method as long as the mechanical state of the brain phantom is consistent regardless of the presence or absence of the skull. This research

has a significant potential for the noninvasive acquisition of the viscoelasticity and fluidity of the soft matters in the detection of crustal movement, material structure, and brain diseases.

ACKNOWLEDGMENTS

This work is supported by the National Natural Science Foundation of China under Grants No. 81827801, No. 81771854, No. 11874049, and No. 11474229.

[1] C. J. Wolfe, S. C. Solomon, G. Laske, J. A. Collins, R. S. Detrick, J. A. Orcutt, D. Bercovici, and E. H. Hauri, Mantle shear-wave velocity structure beneath the Hawaiian hot spot, Science **326**, 1388 (2009).

[2] X. Li, L. Lu, J. Li, X. Zhang, and H. Gao, Mechanical properties and deformation mechanisms of gradient nanostructured metals and alloys, Nat. Rev. Mater. **5**, 706 (2020).

[3] K. Laksari, M. Kurt, H. Babaee, S. Kleiven, and D. Camarillo, Mechanistic Insights Into Human Brain Impact Dynamics through Modal Analysis, Phys. Rev. Lett. **120**, 138101 (2018).

[4] M. Fatemi and J. F. Greenleaf, Ultrasound-stimulated vibro-acoustic spectrography, Science **280**, 82 (1998).

[5] J. Aichele, B. Giammarinaro, M. Reinwald, G. Le Moign, and S. Catheline, Capturing the Shear and Secondary Compression Waves: High-Frame-Rate Ultrasound Imaging in Saturated Foams, Phys. Rev. Lett. **123**, 148001 (2019).

[6] Y. Jiang, G. Li, L. Qian, S. Liang, D. Michel, and Y. Cao, Measuring the linear and nonlinear elastic properties of brain tissue with shear waves and inverse analysis, Biomech. Model. Mechanobiol. **14**, 1119 (2015).

[7] F. C. Meral, T. J. Royston, and R. L. Magin, Surface response of a fractional order viscoelastic halfspace to surface and subsurface sources, J. Acoust. Soc. Am. **126**, 3278 (2009).

[8] H. Zhang, Y. Wang, and M. F. Insana, Ramp-hold relaxation solutions for the KVFD model applied to soft viscoelastic media, Meas. Sci. Technol. **27**, 025702 (2016).

[9] H. Zhang, Q. Zhang, L. Ruan, J. Duan, M. Wan, and M. F. Insana, Modeling ramp-hold indentation measurements based on Kelvin–Voigt fractional derivative model, Meas. Sci. Technol. **29**, 035701 (2018).

[10] S. Cheng, E. C. Clarke, and L. E. Bilston, Rheological properties of the tissues of the central nervous system: A review, Med. Eng. Phys. **30**, 1318 (2008). special issue to commemorate the 30th anniversary of Medical Engineering & Physics

[11] K.-J. Streitberger, E. Wiener, J. Hoffmann, F. B. Freimann, D. Klatt, J. Braun, K. Lin, J. McLaughlin, C. Sprung, R. Klingebiel, and I. Sack, In vivo viscoelastic properties of the brain in normal pressure hydrocephalus, NMR Biomed. **24**, 385 (2011).

[12] E. L. Carstensen, K. J. Parker, and R. M. Lerner, Elastography in the management of liver disease, Ultrasound Med. Biol. **34**, 1535 (2008).

[13] Éric Bavu, J.-L. Gennisson, M. Couade, J. Bercoff, V. Mallet, M. Fink, A. Badel, A. Vallet-Pichard, B. Nalpas, M. Tanter, and S. Pol, Noninvasive in vivo liver fibrosis evaluation using supersonic shear imaging: A clinical study on 113 hepatitis C virus patients, Ultrasound Med. Biol. **37**, 1361 (2011).

[14] L. V. Hiscox, C. L. Johnson, E. Barnhill, M. D. J. McGarry, J. Huston, E. J. R. van Beek, J. M. Starr, and N. Roberts, Magnetic resonance elastography (MRE) of the human brain: Technique, findings and clinical applications, Phys. Med. Biol. **61**, R401 (2016).

[15] E. Macé, I. Cohen, G. Montaldo, R. Miles, M. Fink, and M. Tanter, In vivo mapping of brain elasticity in small animals using shear wave imaging, IEEE Trans. Med. Imaging **30**, 550 (2011).

[16] Z. S. Xu, R. J. Lee, S. S. Chu, A. Yao, M. K. Paun, S. P. Murphy, and P. D. Mourad, Evidence of changes in brain tissue stiffness after ischemic stroke derived from ultrasound-based elastography, J. Ultrasound Med. **32**, 485 (2013).

[17] D. Chauvet, M. Imbault, L. Capelle, C. Demene, and M. Tanter, In vivo measurement of brain tumor elasticity using intraoperative shear wave elastography, Ultraschall in der Medizin **37**, 584 (2015).

[18] R. Muthupillai, D. J. Lomas, P. J. Rossman, J. F. Greenleaf, A. Manduca, and R. L. Ehman, Magnetic resonance elastography by direct visualization of propagating acoustic strain waves, Science **269**, 1854 (1995).

[19] S. A. Kruse, G. H. Rose, K. J. Glaser, A. Manduca, J. P. Felmlee, C. R. Jack, and R. L. Ehman, Magnetic resonance elastography of the brain, NeuroImage **39**, 231 (2008).

[20] J. Huston III, M. C. Murphy, B. F. Boeve, N. Fattahi, A. Arani, K. J. Glaser, A. Manduca, D. T. Jones, and R. L. Ehman, Magnetic resonance elastography of frontotemporal dementia, J. Magn. Reson. Imaging **43**, spcone (2016).

[21] M. Muller, J.-L. Gennisson, T. Deffieux, M. Tanter, and M. Fink, Quantitative viscoelasticity mapping of human liver using supersonic shear imaging: Preliminary in vivo feasability study, Ultrasound Med. Biol. **35**, 219 (2009).

[22] F. Sebag, J. Vaillant-Lombard, J. Berbis, V. Griset, J. F. Henry, P. Petit, and C. Oliver, Shear wave elastography: A new ultrasound imaging mode for the differential diagnosis of benign and malignant thyroid nodules, J. Clin. Endocrinol. Metab. **95**, 5281 (2010).

[23] M. Tanter, J. Bercoff, A. Athanasiou, T. Deffieux, J.-L. Gennisson, G. Montaldo, M. Muller, A. Tardivon, and M. Fink, Quantitative assessment of breast lesion viscoelasticity: Initial clinical results using supersonic shear imaging, Ultrasound Med. Biol. **34**, 1373 (2008).

[24] F. G. Mitri, M. W. Urban, M. Fatemi, and J. F. Greenleaf, Shear wave dispersion ultrasonic vibrometry for measuring prostate Shear stiffness and viscosity: An in vitro pilot study, IEEE Trans. Biomed. Eng. **58**, 235 (2011).

[25] C. Demene, J. Robin, A. Dizeux, B. Heiles, M. Pernot, M. Tanter, and F. Perren, Transcranial ultrafast ultrasound localization microscopy of brain vasculature in patients, Nat. Biomed. Eng. **5**, 219 (2021).

[26] A. Y. Ammi, T. D. Mast, I.-H. Huang, T. A. Abruzzo, C.-C. Coussios, G. J. Shaw, and C. K. Holland, Characterization

of ultrasound propagation through ex-vivo human temporal bone, Ultrasound Med. Biol. **34**, 1578 (2008).

[27] L. E. Miller, J. E. Urban, and J. D. Stitzel, Development and validation of an atlas-based finite element brain model, Biomech. Model. Mechanobiol. **15**, 1201 (2016).

[28] L. Sandrin, M. Tanter, S. Catheline, and M. Fink, Shear modulus imaging with 2-D transient elastography, IEEE Trans. Ultrason. Ferroelectr. Freq. Control **49**, 426 (2002).

[29] P. Grasland-Mongrain, R. Souchon, F. Cartellier, A. Zorgani, J. Y. Chapelon, C. Lafon, and S. Catheline, Imaging of Shear Waves Induced by Lorentz Force in Soft Tissues, Phys. Rev. Lett. **113**, 038101 (2014).

[30] C. Bai, M. Ji, A. Bouakaz, Y. Zong, and M. Wan, Design and characterization of an acoustically and structurally matched 3-D-printed model for transcranial ultrasound imaging, IEEE Trans. Ultrason. Ferroelectr. Freq. Control **65**, 741 (2018).

[31] L. Sandrin, M. Tanter, J.-L. Gennisson, S. Catheline, and M. Fink, Shear elasticity probe for soft tissues with 1-D transient elastography, IEEE Trans. Ultrason. Ferroelectr. Freq. Control **49**, 436 (2002).

[32] T. Gallot, S. Catheline, P. Roux, J. Brum, N. Benech, and C. Negreira, Passive elastography: Shear-wave tomography from physiological-noise correlation in soft tissues, IEEE Trans. Ultrason. Ferroelectr. Freq. Control **58**, 1122 (2011).

[33] K. J. Parker, L. S. Taylor, S. Gracewski, and D. J. Rubens, A unified view of imaging the elastic properties of tissue, J. Acoust. Soc. Am. **117**, 2705 (2005).

[34] V. Dutt, R. R. Kinnick, and J. F. Greenleaf, in *1996 IEEE Ultrasonics Symposium Proceedings*, Vol. 2 (1996), p. 1185.

[35] J. L. Fleiss and J. Cohen, The equivalence of weighted kappa and the intraclass correlation coefficient as measures of reliability, Educational Psychological Meas. **33**, 613 (1973).